Positive feedback of marine N2O emissions during past extreme warming

Xiaoxiao Zhao

xzhao@leibniz.uni-kiel.de

Kiel University

Fanny Monteiro

University of Bristol https://orcid.org/0000-0002-8790-0188

Kevin Becker

University of Bremen https://orcid.org/0000-0001-6317-1884

Lukas Dirksen

University of Bremen

Julia Cordes

University of Bremen

Julius Lipp

MARUM, Center for Marine Environmental Science https://orcid.org/0000-0002-4109-3317

Susan Carter

Harvard University

Nathan Rochelle-Bates

University of St Andrews

Emily Hollingsworth

University of Southampton https://orcid.org/0000-0002-7067-6837

Morgan Jones

Umeå University https://orcid.org/0000-0003-3047-0751

Bo Schultz

Museum Salling - Fur Museum

Alexander Dickson

Royal Holloway, University of London

Mustafa Kaya

RWTH Aachen University https://orcid.org/0000-0003-2966-5092

Ferris Güldner

Kiel University

Eva Stüeken

University of St Andrews https://orcid.org/0000-0001-6861-2490

Gordon Inglis

University of Southampton https://orcid.org/0000-0002-0032-4668
Richard Pancost
University of Bristol
Kai Hinrichs
University of Bremen
Ann Pearson
Harvard University
Felix Elling
Harvard University https://orcid.org/0000-0003-0405-4033

Physical Sciences - Article

Keywords:

Posted Date: February 10th, 2026

DOI: https://doi.org/10.21203/rs.3.rs-8636592/v1

Additional Declarations: There is **NO** Competing Interest.

Positive feedback of marine N_2O emissions during past extreme warming

Xiaoxiao Zhao[1*], Fanny M. Monteiro[2,16], Kevin W. Becker[3,4,5], Lukas Dirksen[5], Julia Cordes[5], Julius S. Lipp[5,6], Susan J. Carter[7], Nathan Rochelle-Bates[8], Emily Hollingsworth[9], Morgan T. Jones[10,11], Bo Pagh Schultz[12], Alexander J. Dickson[13], Mustafa Kaya[14], Ferris Güldner[1], Eva Stüeken[8], Gordon N. Inglis[9], Rich Pancost[15], Kai-Uwe Hinrichs[5,6], Ann Pearson[7], Felix J. Elling[1*]

[1]Leibniz-Laboratory for Radiometric Dating and Stable Isotope Research, Kiel University, 24118, Germany
[2]BRIDGE, School of Geographical Sciences, University of Bristol, BS8 1SS, UK
[3]Faculty of Biology/Chemistry, University of Bremen, 28359 Bremen, Germany
[4]GEOMAR Helmholtz Centre of Ocean Research Kiel, 24148 Kiel, Germany
[5]MARUM Center for Marine Environmental Sciences, University of Bremen, 28334, Germany
[6]Faculty of Geosciences, University of Bremen, 28359 Bremen, Germany
[7]Department of Earth and Planetary Sciences, Harvard University, MA 02138, USA
[8]School of Earth and Environmental Sciences, University of St Andrews, KY16 9TS, UK
[9]School of Ocean and Earth Science, University of Southampton, Southampton, UK
[10] Department of Ecology, Environment and Geoscience, Umeå University, 901 87 Umeå, Sweden
[11]University of Oslo, Departments of Geosciences, Sem Sælands vei 1, 0371, Oslo, Norway
[12]Museum Salling, Fur Museum, Nederby 28, 7884 Fur, Denmark
[13]Centre for Climate, Ocean and Atmosphere, Department of Earth Sciences, Royal Holloway University of London, Egham, Surrey, TW20 0EX, UK
[14]Geological Institute, RWTH Aachen University, Aachen, Germany
[15]Organic Geochemistry Unit, School of Earth Sciences, School of Chemistry, Cabot Institute for the Environment, University of Bristol, Bristol, UK
[16]Centre for ice, Cryosphere, Carbon and Climate (iC3), Department for Geosciences, UiT the Arctic University of Norway, Tromsø, Norway

* Corresponding authors: xzhao@leibniz.uni-kiel.de, felling@leibniz.uni-kiel.de

Abstract: The Paleocene–Eocene Thermal Maximum (PETM; 55.9 million years ago) was a rapid, CO_2-driven climate polycrisis, with global warming of 5-6°C[1,2], ocean acidification[3-5], and deoxygenation[6-8]. These stresses may have affected marine nitrogen cycling, particularly nitrification—a major source of nitrous oxide (N_2O) [9] that remains underexplored on geological timescales. By integrating proxy records with Earth System modeling, we show that nitrification globally increased by ~56% during the PETM. Inhibiting effects of ocean deoxygenation[10] and acidification[11] on nitrification were outweighed by increased ammonium supply and nitrifier niche expansion. Enhanced nitrification led to a ~290% increase in total marine N_2O production, contributing 0.3-1.4°C of warming during the PETM. Our results highlight a strong, positive climatic feedback from nitrogen cycle perturbations under extreme global warming, ocean deoxygenation and acidification.

Nitrogen (N) is a fundamental element of life and a key limiting nutrient in marine ecosystems [12,13], where it's availability is regulated by a complex network of microbially mediated redox reactions[12]. Climatic and environmental stress, such as from global warming, ocean acidification and deoxygenation can perturb these processes, alter the functioning of the N cycle and feed back on the ecosystem and climate. Among these processes, nitrification—the two-step oxygen-dependent oxidation of ammonia into nitrite and then nitrate ($NH_3 \rightarrow NO_2^- \rightarrow NO_3^-$) performed by archaea and bacteria—occupies a central position within the marine N cycle. It links the production of bioavailable nitrogen via N_2 fixation ($N_2 \rightarrow NH_4^+$) to its removal by denitrification (NO_2^- or $NO_3^- \rightarrow N_2$) and anaerobic ammonium oxidation (anammox; $NO_2^- + NH_4^+ \rightarrow N_2$). Additionally, nitrification constitutes one of the main biological sources of nitrous oxide (N_2O)[9], a potent greenhouse gas[14] With a modern global warming potential 273 times higher than carbon dioxide (CO_2)[15]. As nitrification rate depends on both oxygen availability and the pH-sensitive NH_3/NH_4^+ balance[16], it is highly responsive to changes in ocean chemistry: acidification suppresses NH_3 availability[11], while competition with phytoplankton and low oxygen supply are thought to further limit nitrifier activity[10]. CO_2-driven climatic perturbations such as warming, deoxygenation, and acidification therefore have the potential to disrupt nitrification and alter N_2O production, yet the consequences of such forcing, particularly as a combined 'polycrisis', remain poorly understood on geological timescales.

The Paleocene–Eocene Thermal Maximum (PETM, ~56 million years ago) represents the most rapid and extreme CO_2-driven global warming event of the Cenozoic[1,2]. As a deep-time analogue for anthropogenic warming[1], it offers a unique window into investigating biogeochemical feedbacks under extreme climatic stress, including warming[1], ocean acidification[3-5], and deoxygenation[6-8]. Yet, the response of the marine nitrogen cycle, controlled by microbial redox processes and ocean oxygenation, remains poorly constrained, especially at the global scale. Previous reconstructions were based on spatially limited records of nitrogen isotopic composition ($\delta^{15}N$) of bulk or fossil-bound organic matter[17-20]. While overall trends in the nitrogen cycle were captured by these studies, changes in specific nitrogen cycle pathways are still lacking due to methodological constraints, such as overlapping isotopic effects obscuring processes like nitrification[21]. This gap limits our ability to understand nitrogen-cycle feedbacks to warming and to assess their contribution to Earth system sensitivity.

In this study, we resolve nitrogen cycle feedbacks by reconstructing changes in marine nitrogen cycle processes during the PETM using integrated biomarker, isotopic, and numerical modelling approaches. We analyzed biomarkers specific for nitrification and anammox together with bulk nitrogen isotope data ($\delta^{15}N_{bulk}$) from eight globally distributed sites, revealing spatiotemporal variations in nitrogen cycling across the PETM. We place these proxy-based reconstructions in a global context by combining them with simulations from a 3-D Earth system model of intermediate complexity, cGENIE, equipped with a nitrogen cycling

module. This multiproxy–model framework provides new insights into marine nitrogen cycling, with particular emphasis on the role of nitrification and consequent N_2O emissions under extreme climatic perturbation. Collectively, our results indicate that the marine nitrogen cycle acted as positive feedback during the PETM and contributed significantly to global warming.

PETM nitrification intensified globally

To track changes in nitrification across the PETM, we quantified mass accumulation rates of crenarchaeol (MAR_{cren}) (more details in Supplementary Text). Crenarchaeol is a lipid biomarker uniquely produced by ammonia-oxidizing archaea (AOA) [22], the dominant ammonia oxidizers in the ocean[23]. Crenarchaeol was detected at all but one study site (Qimugen Fm), where limited sample availability precluded analysis (Fig. 1). MAR_{cren} increases at almost all sites during the PETM compared to the pre-PETM (Fig. 1). Persistent increases in MAR_{cren} were observed in the Arctic Ocean, the northern Peri-Tethys, the North Sea, the New Jersey shelf, and the equatorial Atlantic (Fig. 1). In contrast, no substantial changes were detected in the Tasman Sea or the North-West Atlantic, indicating a spatially heterogeneous response of the nitrogen cycle. Because ammonia oxidation is the rate-limiting step of nitrification and AOA are obligate chemoautotrophs[24,25], we suggest that the increase in MAR_{cren} reflects both increased nitrification activity and increased AOA biomass flux to sediments. Preservation biases and temperature effects on crenarchaeol production are unlikely to have driven these trends (Supplementary Text, Extended Data Fig. S1). Despite this regional variability, the widespread increase in MAR_{cren} indicates global intensification of nitrification during the PETM.

To overcome the spatial constraints of our proxy dataset and quantify global-scale nitrification fluxes, including deep ocean regions represented by only two study sites, we compared our proxy data with simulations from the cGENIE Earth system model coupled with a nitrogen cycle module[26]. The model was configured with an atmospheric pCO_2 of 556 ppm for the pre-PETM (2×pre-industrial CO_2), and 1668 ppm for the PETM (6× pre-industrial CO_2), together with a 50% increase of the phosphate inventory[6]. Model results broadly align with the proxy data (Fig. 2): regions showing larger MAR_{cren} increases, such as the central Peri-Tethys, also exhibit higher modelled nitrification increases. Enhanced nitrification inferred for the Arctic Ocean and the North Sea from proxy data, however, cannot be resolved in the model due to its limited spatial resolution, highlighting the utility of complementary proxy and modelling approaches. Overall, the model indicates a ~56% global increase in nitrification during the PETM (Fig. 2, Table 1), consistent with elevated MAR_{cren}. This evidence for globally intensified nitrification is unexpected given evidence for ocean acidification and deoxygenation during the PETM, which would be expected to have inhibited nitrification.

Deoxygenation expanded nitrifier niches

Ambient oxygen concentration is a key regulator of both nitrification, which requires O_2, and nitrogen loss processes like anammox and denitrification, which require its absence, thus affecting the balance of the marine nitrogen cycle. To reconstruct subsurface-ocean oxygenation during the PETM, we analyzed Bacteriohopanetetrol-*x* (BHT-*x*), a lipid biomarker uniquely produced by planktonic anammox bacteria[27-30] and its abundance relative to BHT, a biomarker produced by various aerobic and anaerobic bacteria (BHT-*x* ratio)[27,30]. Because anammox bacteria require low-oxygen conditions ($[O_2]<50$ μM), the BHT-*x* ratio serves as a proxy for suboxic to anoxic conditions in the upper ocean[28]. BHT-*x* was detected at three sites where sufficient amounts of sediment were available to allow its analysis (Arctic Ocean, New Jersey shelf and Tasman Sea) (Extended Data Table 2). Among these, only the Arctic Ocean exhibited a high BHT-*x* ratio (>0.2) during the PETM, indicating increased anammox activity and low dissolved O_2 concentrations ($[O_2]<50$ μM; Fig. 1)[30] (more details in Supplementary Text). Complementary cGENIE simulations indicate widespread but spatially heterogeneous subsurface deoxygenation during the PETM (Table 1, Fig. 2): the Peri-Tethys Sea experienced near-complete oxygen loss, $[O_2]$ in the Atlantic and southeastern Pacific declined by ~50–80%, and in the open Pacific by ~20–40%. Using $[O_2] < 10$ μM as anoxic and 10–60 μM as hypoxic thresholds[31], the model infers anoxia in the Peri-Tethys and hypoxia in the North Atlantic, consistent with low BHT-*x* ratios in the New Jersey shelf (suggesting $[O_2]>50$ μM; Fig. 2, Extended Data Fig. S2). Similarly, the Tasman Sea shows both low BHT-*x* ratios and modelled $[O_2]$ levels above the hypoxic threshold. The model–proxy correspondence indicates spatially heterogeneous yet pervasive upper-ocean oxygen depletion during the PETM.

Although nitrification requires oxygen, its intensification during the PETM (Table 1), even under declining subsurface $[O_2]$ (Fig. 2), suggests that deoxygenation did not limit nitrifier activity. Similar patterns are observed in modern low-$[O_2]$ systems such as the Black Sea and the eastern tropical Pacific, where ammonium accumulates in the deep anoxic zones[32,33]. Nitrifiers are adapted to low-$[O_2]$ conditions due to their high oxygen affinity[34,35] and tend to be most active in aphotic, low-$[O_2]$ transition zones above anoxic waters[36,37]. Under these conditions, where $[O_2]$ is sufficient to support metabolism but competition from phytoplankton is reduced, nitrifiers take advantage of high NH_4^+ flux from the underlying anoxic zone[38,39]. Therefore, global ocean deoxygenation during the PETM likely broadened ecological niches for marine nitrifiers by enhancing NH_4^+ supply in low-O_2 environments.

Ammonium fueled nitrification despite low pH

We propose that in concert with niche expansion, elevated NH_4^+ availability was the major driver of amplified marine nitrification rates during the PETM. Evidence for increased NH_4^+ comes from both cGENIE simulations and $\delta^{15}N_{bulk}$ records (Fig. 2, Supplementary Text). cGENIE simulations show globally increased seawater NH_4^+ concentrations during the PETM, with the largest absolute values and increases in the northern Peri-Tethys (Fig. 2c, Extended Data Fig. S2). Globally, NH_4^+ assimilation by phytoplankton increased by ~50% (Table 1). This pattern is reflected in $\delta^{15}N_{bulk}$ values, which decrease markedly during the PETM, reaching below -1‰ in the equatorial Atlantic, northern Peri-Tethys[17], and North Sea (Fig. 1), Values of $\delta^{15}N_{bulk}$ < -2‰ indicate substantial NH_4^+ accumulation in anoxic waters and its uptake by phytoplankton. This suggests a fundamental shift in fixed nitrogen availability and sources during the PETM.

The elevated NH_4^+ supply during the PETM was likely driven by increased nitrogen fixation and productivity[40,41], stimulated by enhanced phosphorus supply[41], together with intensified remineralization, as supported by the cGENIE model (Table 1, Extended Data Fig. S2). Subsurface deoxygenation and expansion of anoxic zones fostered the accumulation NH_4^+ [42]. Semi-enclosed basins such as the Peri-Tethys, where topographic constraints limited exchange with oxic waters, experienced the strongest deoxygenation and NH_4^+ accumulation. This fostered high nitrification rates and NH_4^+ uptake by phytoplankton, as reflected by negative $\delta^{15}N_{bulk}$ values (Fig. 2). In contrast, decreases in $\delta^{15}N$ values to ~0 to 2‰ in the Arctic Ocean suggest enhanced nitrogen loss and NH_4^+ accumulation without significant phytoplankton assimilation (Supplementary Text). Moderate $\delta^{15}N_{bulk}$ decreases in other regions (e.g., New Jersey shelf, eastern Peri-Tethys) likely reflect enhanced nitrogen loss and/or increased reliance on N_2 fixation (producing biomass/NH_4^+ with $\delta^{15}N$ of ~0 to 1‰). Together, isotopic and model evidence consistently point to a global-scale increase in NH_4^+ availability that would have fueled nitrification, despite regional variability and enhanced nitrogen loss.

The stimulatory effects of enhanced NH_4^+ availability on nitrification observed during the PETM could have been offset by ocean acidification. Acidification can inhibit nitrification by shifting the $NH_3 \leftrightarrow NH_4^+$ equilibrium towards NH_4^+[43], reducing NH_3 availability for ammonia oxidizers (Fig. 3), as suggested by experimental evidence[11,44]. However, these experiments assessed only pH effects and did not consider feedbacks involving total ammonia nitrogen availability (TAN; the sum of [NH_3] and [NH_4^+])[11,45]. To evaluate the combined effects of pH and TAN on nitrification, we applied a Michaelis–Menten formulation in which nitrification rates depend on NH_3 availability, regulated by both pH-dependent equilibrium[11] and TAN (Supplementary Text, Extended Data Fig. S4). Within this framework, a PETM pH decline of 0.46 units[45] would have reduced [NH_3] by ~64%, lowering nitrification to ~36% of pre-PETM levels if TAN remained constant. However, increases in TAN can readily compensate for this inhibitory effect: for example, a two-fold increase in TAN would offset the

reduction in nitrification associated with a 0.46-unit pH decrease. To reproduce the ~55% global increase in nitrification simulated by cGENIE (Table 1), a ~4.4-fold increase in TAN availability would be sufficient in this simplified scenario. This implies that intensified remineralization and TAN buildup during the PETM outweighed the inhibitory effect of acidification.

Nitrification amplified PETM warming via N_2O

Nitrification has a major climatic impact through its production of N_2O as a side-product[9]. Yet, marine N_2O fluxes and their interaction with climatic and ocean biogeochemistry remain unconstrained beyond the ice core record (~800 kyr)[46], leaving deep-time variability largely unexplored. During the PETM, intensified nitrification likely enhanced N_2O emissions, while deoxygenation may have further amplified N_2O yield from nitrification[37,47,48]. Additionally, anoxia would have enhanced heterotrophic denitrification, another major source of oceanic N_2O[49].

We estimated N_2O emission rates during and preceding the PETM by applying an oxygen- and depth-partitioning scheme of N_2O emissions[50] to cGENIE-simulated nitrification rates and $[O_2]$. This approach represents a novel implementation of this empirical scheme within a global Earth system model. With this approach, we estimated that oceanic N_2O production by nitrifiers increased by ~74% (0.4 TgN yr^{-1}) during the PETM (Table 1). Amplified nitrification also enhanced the supply of oxidized nitrogen substrates (NO_2^-, NO_3^-) for denitrification, which increased N_2O production from denitrification by ~466% (3.2 TgN yr^{-1}). Combined, amplified nitrification and denitrification resulted in 3.6 TgN yr^{-1} higher N_2O emissions compared to the pre-PETM ocean. The corresponding additional effective radiative forcing is estimated at 0.4-0.6 W m^{-2}, depending on background greenhouse gas levels (Extended Data Fig. S6). Under PETM-like atmospheric compositions, this forcing would have elevated atmospheric N_2O concentration by ~195 ppb relative to pre-PETM levels. Across plausible equilibrium climate sensitivities (ECS = 2.5–9 °C per CO_2 doubling), this marine N_2O forcing could have contributed ~0.3–1.4 °C of additional warming, with higher ECS producing stronger warming. Given evidence for elevated ECS during the PETM compared to the modern[51-53], the N_2O-induced warming likely falls within the upper end of this range, representing a strong, positive feedback to PETM warming.

These estimates are conservative, as low $[O_2]$ enhances N_2O yield from nitrification and because ocean acidification amplifies N_2O yield from both ammonia oxidation and denitrification[37,47,48,54]. N_2O production is therefore expected to increase further under PETM-like suboxic and acidified conditions. In addition, the Arctic Ocean and the North Sea are not accounted for in our approach due to the model resolution. However, the enhanced nitrification and

reduced oxygenation in these regions indicated by our proxy data suggests additional N_2O emissions from these regions (Fig. 1). Beyond the oceans, the terrestrial biosphere is the dominant natural source of modern N_2O in the modern environment–a source that was likely also sensitive to PETM climate forcing. An intensified hydrological cycle and amplified wet-dry variability during the PETM, driven by more episodic precipitation[40], might have amplified terrestrial N_2O fluxes[55]. The combined greenhouse forcing from marine and terrestrial N_2O would help resolve a major conundrum by explaining why CO_2 emissions alone are insufficient to account for the full 5-6 °C warming observed for the PETM[56], with marine N_2O emissions potentially contributing ~5-30% of the total warming[52,57]. Future efforts to better quantify global N_2O concentrations during the PETM, especially for terrestrial sources, are essential to refine estimates of Earth's climate sensitivity and the role of the N cycle in modulating climate. Overall, our findings highlight the complex feedbacks between marine nitrogen cycle and climate during the PETM 'polycrisis', identifying nitrification as a key amplifier of greenhouse gas forcing. Our observations are likely applicable to other Cenozoic periods of extreme warming events and provide insights into the long-term consequences of global warming, ocean deoxygenation and acidification under ongoing climate change.

Acknowledgments: This research used samples provided by the Ocean Drilling Program (ODP) and the International Ocean Discovery Program (IODP).

Funding:

Deutsche Forschungsgemeinschaft grants 441217575 and 527682349 (FJE)

European Association of Organic Geochemistry through the Elsevier Research Scholarship (XZ)

European Consortium for Ocean Research Drilling through an ECORD research grant (XZ)

UK Research and Innovation Natural Environment Research Council grant TONIC, NE/V01823X/1 (FMM)

Research Council of Norway through its PETROMAKS program, grant 336293 PALMAR (MTJ)

Royal Society Dorothy Hodgkin Fellowship Renewal DHF\R\241007 (GNI)

Deutsche Forschungsgemeinschaft through the Cluster of Excellence "The Ocean Floor – Earth's Uncharted Interface" (project 390741603)(K-UH)

US-National Science Foundation grants OCE-1702262 and OCE-1843285 (AP).

Author contributions:

Conceptualization: XZ, FJE

Methodology: XZ, FMM, FJE, KWB, KUH, AP

Investigation: XZ, FJE, LD, JC, JSL, SJC, NRB, EH, GNI

Formal analysis: XZ, FMM

Visualization: XZ

Funding acquisition: FJE, XZ, FMM, MTJ, GNI, K-UH, AP

Resources: FJE, FMM, MTJ, BPS, AJD, KWB, MK, ES, GNI, RP, KUH, AP

Supervision: FJE, FMM

Writing – original draft: XZ, FMM, FJE

Writing – review & editing: All authors

Competing interests: Authors declare that they have no competing interests.

Data and materials availability: All data are available in the main text or the supplementary materials.

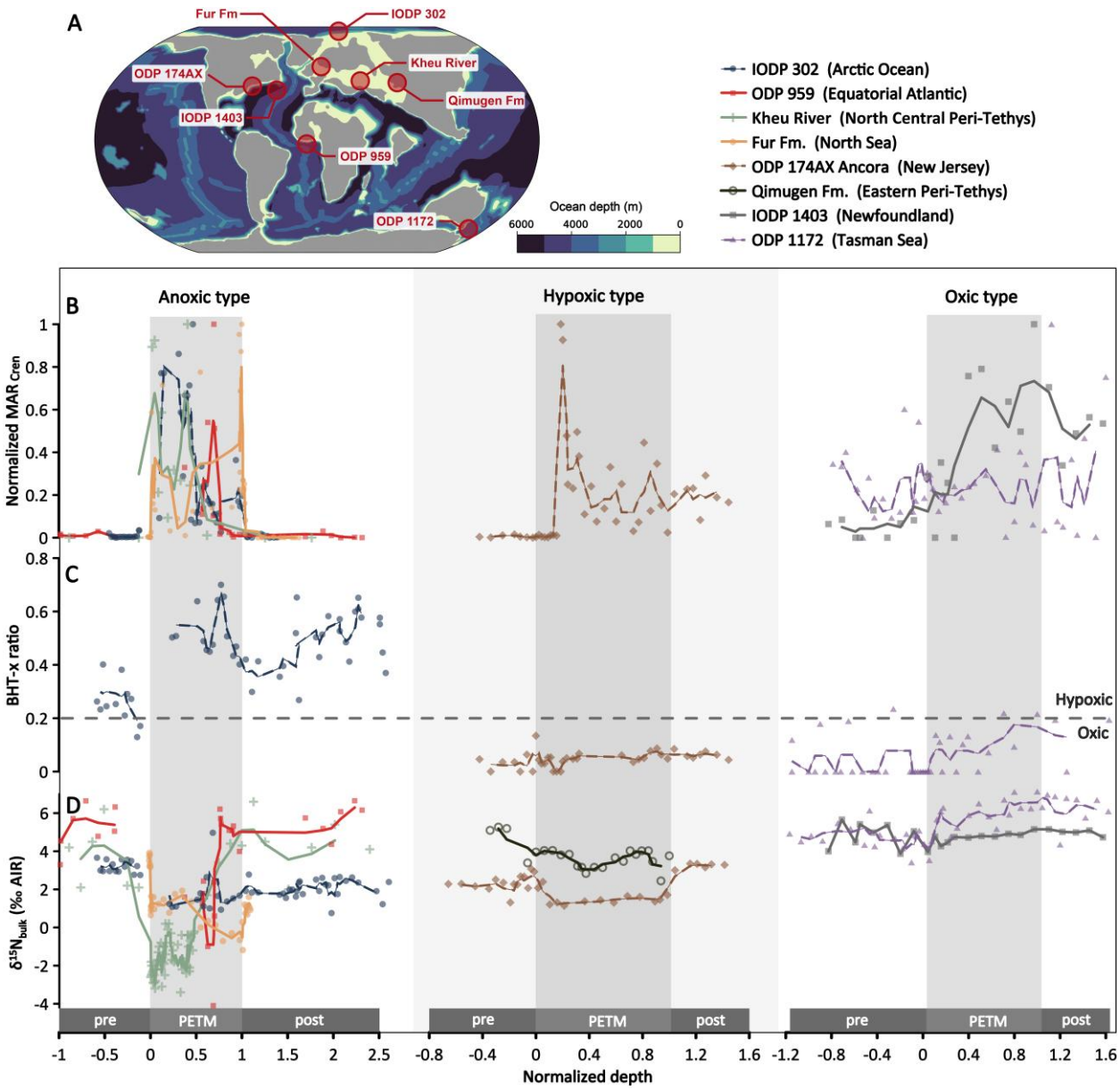

Fig. 1. Proxy records indicating changes in the marine nitrogen cycle during the PETM. A Sampling locations and plate configuration during the late Palaeocene (ca. 55 Ma)[58]; **B,** Normalized crenarchaeol mass accumulation rate (MAR_{cren}), a biomarker of ammonia-oxidizing archaea and a proxy for nitrification, normalized to the maximum value at each site; **C,** Bacteriohopanetetrol-*x* (BHT-*x*) ratio, a biomarker produced by anaerobic ammonium-oxidizing bacteria and a proxy for low O_2 concentrations (BHT-*x* ratio >0.2 suggests <50 µm O_2); **D**, bulk sediment $\delta^{15}N$ ($\delta^{15}N_{bulk}$), integrates nitrogen inputs, losses, and the relative contributions of fixed nitrogen species such as NO_3^- and NH_4^+ to phytoplankton biomass production. $\delta^{15}N_{bulk}$ data for the Kheu River site are from ref.[17]. For ease of visualization, sediment depths for all sites are normalized to the onset of the PETM, assuming constant sedimentation rate. Supplementary Fig. 1 shows the same data adjusted for sedimentation rates. Sites are grouped into three categories (anoxic, suboxic and oxic)

based on an integrated assessment of BHT-*x* ratio, $\delta^{15}N_{bulk}$ values and cGENIE-simulated oxygen levels (anoxic: $[O_2]<10$ µM; hypoxic: $10<[O_2]<60$ µM; oxic: $[O_2]>60$ µM). Solid curves represent 3-point running averages. The grey shadings indicate the carbon stable isotopic excursion and thus the approximate duration of the event (~170 kyr). Abbreviations: pre: pre-PETM; post: post-PETM.

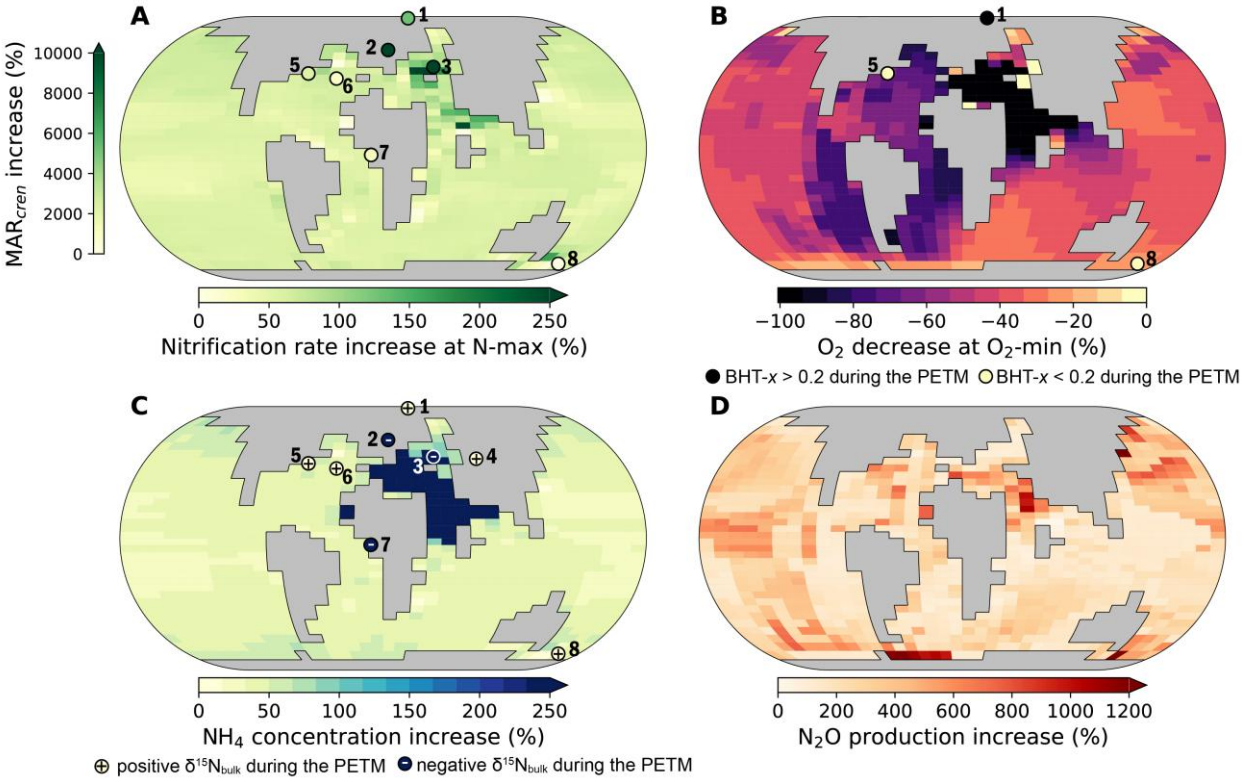

Fig. 2. Proxy- and cGENIE model-based reconstructions of nitrogen cycle changes during the PETM relative to pre-PETM conditions. **A**, Modelled percent change in nitrification rates at the nitrification maximum depth (N-max), overlaid with site-specific increases in Crenarchaeol mass accumulation rate (MAR$_{cren}$) in circle (in colour scale); **B**, Percent decrease in oxygen concentration at the modelled oxygen minimum depth (O_2-min). Black circles indicate sites with increased BHT-*x* ratios, a proxy for anaerobic ammonium oxidation (anammox) and hypoxia during the PETM; yellow circles indicate no change; **C**, Proxy- and model-based percent change in depth-integrated NH_4^+ concentration. Circles denote negative (-) and positive (+) $\delta^{15}N_{bulk}$ values during the PETM; **D**, Reconstructed percent increase in N_2O production from nitrification and denitrification. Numbers refer to sampling sites: 1. Arctic Ocean (IODP 302); 2. North Sea (Fur Fm); 3. North Central Peri-Tethys (Kheu River); 4. Eastern Peri-Tethys (Qimugen Fm); 5. New Jersey Shelf (ODP 174AX Ancora); 6. Newfoundland (IODP 1403); 7. Equatorial Atlantic (ODP

959); 8. Tasman Sea (ODP 1172). The Arctic Ocean is masked, as the model configuration does not resolve physical circulation appropriately in this region.

Table 1. cGENIE model results of ocean biogeochemistry during and preceding the PETM compared to modern observations. Anoxia is defined as $[O_2] < 10$ μM. References for modern observations are listed in parentheses.

Variable	Unit	Modern (Observed)	Pre-PETM	PETM
Global inventories				
Atmospheric CO_2		1 × CO_2	2× CO_2	6× CO_2
Oceanic phosphate		1 × PO_4^{3-}	0.5× PO_4^{3-}	0.75× PO_4^{3-}
Ocean anoxia	% volume	<0.1	<0.1	1.3
Marine biological rates				
Export production	Gt C y^{-1}	5–20	4	6
Nitrification	Tg N y^{-1}	1100-5400 [59]	1402	2183
Nitrogen loss	Tg N y^{-1}	120–240	83	259
NH_4^+ assimilation	Tg N y^{-1}		650	1011
Remineralization	Gt C y^{-1}		12	19
Ocean fixed N inventory				
NH_4^+	μmol kg^{-1}	<0.1 [12]	<0.1	0.1
NO_3^-	μmol kg^{-1}	30 [12]	15.9	21.3
Total fixed N	μmol kg^{-1}	34 [12]	15.9	21.4
N_2O emission				-
Nitrification	TgN yr^{-1}	1.1 [50]	0.57	0.99
Denitrification	TgN yr^{-1}	1.6 [50]	0.68	3.85
Total	TgN yr^{-1}	2.9 [50]	1.25	4.84

Methods

Sample description

We sampled the Paleocene-Eocene boundary from the Arctic Ocean (IODP 302, Hole M0004A, cores 28X-32X), North Sea (Fur Formation, Denmark), North Atlantic (ODP Leg 174AX Ancora Site, Hole A/B and IODP Leg 342, Site 1403), equatorial Atlantic (IODP Leg 159, Site 959, Hole D), Peri-Tethys (Kheu River, Northern Caucasus and Qimugen Formation, Mine section, Tarim Basin), and Tasman Sea (ODP Leg 189, Site 1172 Hole D). Detailed information can be found in Extended Data Table 1. The pre-PETM, PETM and post-PETM intervals were defined based on the characteristic negative excursion in the stable isotopic composition of bulk organic carbon ($\delta^{13}C_{org}$)[60].

The data from each record is reported based on depth. For ocean drilling samples from ODP and IODP, composite depth (mcd) was used in order to stratigraphically correlate holes. For Qimugen Fm samples, depth is reported following ref. [61]. For the Fur Fm, depth is normalized relative to Ash layer -33 as a convention[62].

Sample preparation and extraction

Sediment samples were freeze-dried and ground using an agate mortar and pestle or an agate ball mill, and extracted using a Thermo ASE350 accelerated solvent extraction system at 100 ℃ and 100 bar in three steps: 1) DCM:Methanol 1:1 (*v*/*v*); 2) DCM:Methanol 9:1 (*v*/*v*); 3) 100% DCM. Each extraction step included 1) preheating for 2 min, 2) holding at 100℃ for 5 min, 3) cool down, before the extract was collected. The three extracts were then combined into a total lipid extract (TLE), concentrated under a flow of N_2 and stored at -20 ℃. An aliquot of the TLE was separated using combusted silica gel chromatography into F1, F2-5, F6-8, F8.5 and F9-10 fractions. BHPs were contained in F9-10 fraction[63].

Biomarker quantification

1. Crenarchaeol

The TLE was used for (semi-)quantification of crenarchaeol using a coupled high-performance liquid chromatography (HPLC)-mass spectrometry system (MS) consisting of an Agilent 1260 Infinity II series HPLC and an Agilent 6130 mass spectrometer equipped with an atmospheric-pressure chemical ionization interface operated in positive mode. The HPLC method followed ref.[64,65]. The MS was operated in selected ion monitoring mode. To semi-quantify crenarchaeol concentration, we used C_{46}-GTGT as an internal standard and calculated concentrations through an external standard curve, under the assumption that the response of crenarchaeol is proportional to that of C_{46}-GTGT.

We use MAR_{cren} as a proxy for nitrification, with higher MAR_{cren} indicating increased AOA biomass and higher nitrification rate[66,67]. The MAR was calculated

based on sedimentation rates and dry bulk density (Extended Data Table1). Dry bulk density data was obtained from IODP or ODP preliminary reports. The MAR_{cren} (in ng cm^{-2} kyr^{-1}) was calculated as follows:

$MAR_{cren} = LSR * \rho * [Cren]$,

where LSR is the linear sedimentation rate (cm Kyr^{-1}), ρ is the dry bulk density (g cm^{-3}) (Extended Data Table1), and [Cren] is the crenarchaeol concentration, normalized to grams of sediment.

2. Bacteriohopanetetrol

Bacteriohopanetetrol analysis was performed on the polar fraction without derivatization. Analysis of Bacteriohopanetetrol was conducted at the University of Bremen using a Dionex Ultimate 3000RS ultra- HPLC system connected to a Bruker maXis Plus Ultra-High Resolution quadrupole time-of-flight tandem MS (UHR-qTOF-MS) equipped with an ESI ion source operating in positive ion mode (Bruker Daltonik, Bremen, Germany). Chromatographic separation was achieved using an Acquity BEH C18 column (2.1 × 150 mm, 1.7 μm particle size, Waters, Eschborn, Germany) set to a temperature of 30 °C. The separation method is modified from ref. [68,69]. The solvent system consisted of eluent A (MeOH:H_2O; 85:15 (*v*/*v*)) and eluent B (MeOH:isopropanol; 1:1 (*v*/*v*)) with both containing 0.12 % (v/v) formic acid and 0.04 % (v/v) aqueous ammonia. Compounds were eluted with 5% B for 3 min, followed by a linear gradient to 60% B at 12 min and then to 100% B at 50 min and holding at 100% B until 80 min. The column was then equilibrated for 20 min leading to a total run time of 100 min. The flow rate was held constant at 0.2 ml min^{-1}. Mass spectra were acquired in positive ion monitoring of m/z 50 to 2000 and data-dependent fragmentation of the most abundant ions (dynamically selected, typically 3-8) for a total cycle time of 2 s and dynamic exclusion (activation after 5 spectra, release after 15 s). Ion source settings and parameters for detection and fragmentation of bacteriohopanetetrol were optimized while infusing extracts. Every analytical run was mass-calibrated by loop-injection of Agilent ESI-L tune mix and lock mass calibration (m/z 922.0098, added in ESI source) of each mass spectrum, leading to typical mass deviations of < 1-3 ppm.

Bacteriohopanetetrol were identified based on the exact mass of the protonated or ammoniated molecular ions, relative retention time and MS^2 fragmentation, following ref. [69].

3. Carbon and nitrogen isotopes

Samples for bulk carbon and nitrogen analysis (all sites except Fur Fm) were prepared by homogenizing freeze-dried sediment samples using an agate mortar and pestle. For total organic carbon measurements, sediment samples were pre-treated with hydrochloric acid to remove carbonates, washed with ultrapure water, freeze-dried

again and analyzed using a ThermoScientific Flash EA coupled to a Delta V Plus isotope ratio mass spectrometer at Harvard University[70]. Bulk nitrogen isotopic composition was analyzed from untreated, homogenized, and freeze-dried sediment using the same instrument. Standards of known carbon and nitrogen isotopic composition (glutamic acid, tyrosine, USGS-40, USGS-41a) were used for peak size correction and offset correction[71].

Samples from the Fur Fm were prepared and analyzed at the University of St Andrews. After milling with an agate mortar and pestle, dry sediment sample aliquots (~0.5 g) were mixed with 1 M HCl in glass centrifuge tubes and stirred with a glass rod. The tubes were loosely capped and left to react overnight in a fume hood at room temperature. The next day, samples were centrifuged at 700 rpm and the supernatant decanted. The tubes were then re-filled with fresh 1M HCl, stirred with a glass rod and left to react for another ~4 hours, before centrifuging and decanting again. The sample residues were then washed with DI water, stirring with a glass rod, before they were centrifuged and the supernatant decanted. The water wash step was repeated two more times. Sample residues were then dried in an oven at 70°C for 2-3 days, before they were transferred to glass scintillation vials for storage. All glassware used for sample preparation and storage was pre-combusted at 500 °C. For analysis, sample aliquots were weighed into 8 x 5 mm tin capsules and analyzed using an elemental analyser (EA Isolink; Thermo Fisher) coupled via a Conflo IV to a MAT253 isotope ratio mass spectrometer (Thermo Fisher). Measurements were calibrated using the standards USGS-41a and USGS-40. The USGS-62 ($\delta^{13}C$ = -14.72 ± 0.19‰ [1σ], $\delta^{15}N$ = 20.37 ± 0.19‰ [1σ], n=12) and SDo-1 ($\delta^{13}C$ = -30.45 ± 0.2‰ [1σ], $\delta^{15}N$ = -0.50 ± 0.36‰ [1σ], n=4) standards were used to test reproducibility, and the results agree well with published values (USGS-62: $\delta^{13}C$ = -14.79 ± 0.04‰, $\delta^{15}N$ = 20.17 ± 0.06‰ (ref. [68]); SDo-1: δ13C = -30.0 ± 0.1 ‰, δ15N = -0.8 ± 0.3 ‰; Dennen et al., 2006).

All nitrogen and carbon isotopic results are expressed in delta notation ($\delta^{15}N = [(^{15}N/^{14}N)_{sample}/(^{15}N/^{14}N)_{standard}–1]\times1000$) versus air for nitrogen and ($\delta^{13}C = [(^{13}C/^{12}C)_{sample}/(^{13}C/^{12}C)_{standard} - 1] \times 1000$) versus the Vienna Peedee Belemnite (VPDB) standard for carbon.

cGENIE model description

We employed the cGENIE Earth system model of intermediate complexity, with a nitrogen cycling module, combining the configurations established by ref. [6] for the PETM and by ref. [42] for the nitrogen cycle. The model resolves 3-D ocean circulation and biogeochemistry coupled to a 1-D energy balance atmosphere[72]. Ocean biogeochemistry includes the cycling of carbon, oxygen, phosphorus and sulphur following ref. [6], together with the nitrogen cycling developed by Naafs et al.[42]. The nitrogen scheme explicitly represents multiple pools (nitrate, ammonia and organic nitrogen) and pathways, including nitrification, ammonia regeneration from remineralization of organic nitrogen, nitrogen assimilation during photosynthesis, nitrogen fixation and total nitrogen loss. Nitrification is modelled as co-limitated by

temperature, oxygen and ammonia availability[42]. In essence, our model incorporates the nitrogen configuration of Naafs et al.[42] within the updated redox framework of Reinhard et al.[73], as implemented in Behrooz et al.[6], which characterizes remineralization through a continuous series of redox reactions (Extended Data Fig. S3).

To simulate pre-PETM conditions, we applied boundary conditions consistent with earlier studies[6] of 0.5× modern phosphate (PO_4^{3-}) and 2× pre-industrial atmospheric CO_2. For body-PETM conditions, we used 0.75× PO_4^{3-} and 6× CO_2. In cGENIE, phosphate inventory exerts a strong control on marine biogeochemistry by regulating oxygen levels: higher phosphate promotes higher primary production and remineralization, which in turn reduces dissolved oxygen and modulates the nitrogen cycle[42]. An increase in phosphate inventory during the PETM is supported by both weathering proxies and sedimentary records[41]. This configuration effectively reproduces bottom water anoxia and photic zone euxinia, consistent with biomarker evidence such as isorenieratane distributions[6], and captures the spatial patterns and magnitudes of nitrogen cycle perturbations presented in this study. However, the prescribed phosphate inventory should be viewed as an effective model parameter rather than an absolute reconstruction, as the Eocene-like cGENIE configuration lacks iron limitation; consequently, the true phosphate inventory during the PETM may have been higher than implied by the simulations.

Modelled effect of pH and TAN on nitrification rate

We quantified the effect of seawater pH and total ammonia nitrogen (TAN = $[NH_3]$ + $[NH_4^+]$) on ammonia-oxidation (nitrification) assuming Michaelis–Menten kinetics with NH_3 as the substrate:

$$v = \frac{V_{max} \times [NH_3]}{K_m + [NH_3]}$$

v is the nitrification rate, V_{max} is the maximum constant rate of nitrification, K_m is the half-saturation constants for NH_3. The $[NH_3]$ fraction was computed from the Henderson–Hasselbalch relation[11]:

$$\alpha(pH) = \frac{1}{1 + 10^{(pK_a - pH)}}$$

using pK_a=9.25 for sea water at ~25℃. So:

$$[NH_3] = \alpha \cdot TAN$$

For comparison, we normalize to a reference state (pH_0, TAN_0), with pH_0=7.91 according to the reconstructed sea water pH preceding the pre-PETM. And we define the saturation parameter:

$$r = \frac{TAN}{K_m}$$

Therefore, we have the relative response of nitrification rate:

$$\frac{v}{v_0} = \frac{r\alpha}{1+r\alpha} \cdot \frac{1+r_0\alpha_0}{r_0\alpha_0},\ \alpha_0 = \alpha(pH_0)$$

For visualization, we mapped v/v_0 across pH (from 7.2-8.2) and r/r_0 (from 10^{-1}-10) (Extended Data Fig. S4)

Under low substrate condition, we have $[NH_3] \ll K_m (i.e., r\,\alpha \ll 1)$, for which

$$\frac{v}{v_0} = \frac{TAN}{TAN_0} \cdot \frac{\alpha}{\alpha_0} \cdot \frac{K_{m,0}}{K_m}$$

when comparing the same nitrifier community (K_m=$K_{m,0}$),

$$\frac{v}{v_0} = \frac{TAN}{TAN_0} \cdot \frac{\alpha}{\alpha_0}$$

The response of nitrification change is linear to the change of TAN. Accordingly, a 4.34-fold increase in TAN together with a 0.46-unit decrease in pH yields a 1.55-fold increase in the rate relative to pre-PETM under low-substrate availability (Extended Data Fig. S4). Under high-substrate availability, the saturation term $r\alpha$ cannot be neglected; to achieve the same 1.55-fold increase, r/r_0=4.45 is required (Extended Data Fig. S4).

Estimation of marine N_2O emissions

Since the cGENIE model does not explicitly resolve N_2O cycling, we diagnosed oceanic N_2O emissions by combining model-derived rates of nitrification (ammonia oxidation) and nitrogen loss with an oxygen- and depth-dependent partitioning scheme adapted from Wang et al. [50].

For each water column, the depth of the source–sink boundary for N_2O emission was defined as the depth of minimum oxygen concentration (z_b). Only N_2O produced above this boundary was assumed to contribute to atmospheric emissions, while N_2O produced below was assumed to be quantitatively reduced to N_2 and thus not contribute to atmospheric emissions.

For nitrification-derived N_2O, the vertically integrated N_2O flux to the atmosphere at each model grid cell (F_{nitri}; Tg N/m^2/yr) was expressed as:

$$F_{nitri} = r_{N_2O}(O_{2,b}) \int_0^{z_b} R_{nitri}(z) \times Y_{nitri} dz$$

Where R_{nitri} is the model-derived nitrification rate (mol kg^{-1} yr^{-1}), Y_{nitri} is the fractional N_2O yield parameter from nitrification (%) and $r_{N_2O}(O_{2,b})$ is the fraction of residual unreduced N_2O, calculated based on the local $[O_2]$ in each model grid cell. The empirical relationship linking $r_{N_2O}(O_{2,b})$ the residual N_2O fraction to oxygen

concentration at the source–sink boundary was adopted from the observationally constrained curve of Wang et al. [48]. The parameter Y_{nitri} was calibrated by tuning modern cGENIE-modelled N_2O production to match observed global estimates[48] (Extended Data Fig. S5), acknowledging that the model does not distinguish between N_2O production during ammonia oxidation and nitrite oxidation. Here, Y_{nitri} is set to 0.088%, within the range of N_2O yield of nitrifiers from culture experiments[50].

To calculate the N_2O emissions from nitrogen loss, we separated the total nitrogen loss flux (R_{Nloss}) in cGENIE model into sedimentary denitrification, water-column denitrification and anammox. Anammox does not produce N_2O, so that N_2O emissions were calculated only from the denitrification fractions.

As cGENIE does not explicitly distinguish among these nitrogen loss pathways, partitioning was based on local oxygen concentrations and bathymetry First, we assigned any model-derived nitrogen loss occurring within the bottom-layer grid cells to sedimentary denitrification. All remaining nitrogen loss was attributed to the water column. Within the water column, nitrogen loss was further separated into denitrification and anammox according to dissolved oxygen thresholds derived from laboratory and field observations of oxygen-limited zones:

$$f_{deni|pel} = \{0.9,\ O_2 \le 10\ \mu M\ 0.8,\ \ 10 < O_2 \le 60\ \mu M\ 0.7,\ \ O_2 > 60\ \mu M$$

Where $f_{deni|pel}$ denotes the fraction of water-column nitrogen loss as denitrification. The corresponding rates of water-column denitrification and anammox were then calculated as:

$$R_{deni|pel} = f_{deni|pel} R_{Nloss};\ R_{deni|anammox} = (1 - f_{deni|pel}) R_{Nloss}$$

with sedimentary denitrification ($R_{deni|ben}$) equal to R_{Nloss} in bottom cells.

Nitrous oxide production from total denitrification (P_{deni}) was calculated using constant yield factors (Y)

$$P_{deni} = R_{deni|pel} Y_{deni|pel} + R_{deni|ben} Y_{deni|ben}$$

Where $Y_{deni|pel} = 8\%\ and\ Y_{deni|ben} = 0.1\%$. $Y_{deni|pel}$ represent the N_2O yields from water-column denitrification and sedimentary denitrification (%), respectively.

The vertically integrated N_2O flux to the atmosphere from denitrification at each grid point was expressed as:

$$F_{deni} = r_{N_2O}(O_{2,b}) \int_0^{z_b} P_{deni}(z) dz$$

Global marine N_2O atmospheric emissions were obtained by integrating grid-cell fluxes over the ocean surface area and converting to units of Tg N yr^{-1}.

Calculation of the marginal radiative forcing of marine N_2O emissions

We estimated the additional radiative forcing caused by increased marine N_2O emissions during the PETM. Because atmospheric N_2O concentration during the PETM cannot be directly reconstructed from proxies, we calculated the marginal radiative forcing (ΔF_{nitri}) of N_2O emissions from nitrification and denitrification from calculation above. We first converted the additional oceanic N_2O flux into the corresponding steady-state atmospheric concentration rise, assuming a constant global N_2O lifetime of 116 years [74]. The resulting change in the N_2O mixing ratio was inserted into the IPCC Sixth Assessment Report (IPCC AR6) parameterization linking CO_2, CH_4 and N_2O to radiative forcing[73]. Finally, this forcing was converted to an approximate surface temperature response using a standard climate-sensitivity relationship.

Several factors influence the results: First, background CO_2 and CH_4 levels set the radiative environment and affect how strongly N_2O absorbs infrared radiation. To assess how different background CO_2 and CH_4 level influence results, sensitivity tests were conducted in a CO_2 range from 900-3000 ppm and a CH_4 range from 1000-3500 ppb (Extended Data Fig. S6). Similarly, the PETM background N_2O level can also affect the results. Sensitivity tests using 270–400 ppb backgrounds show that the forcing decreases by roughly 4–16 % as the baseline N_2O increases. Second, the atmospheric lifetime of N_2O controls how much its concentration increases for a given emission change. Here, we use mean atmospheric lifetime of N_2O 116 years, following the IPCC AR6[74]. However, we acknowledge that it is unconstrained if this modern-day chemical lifetime may hold under PETM conditions. Third, equilibrium climate sensitivity (ECS) translates the forcing into temperature but remains uncertain both in the modern and in the geological past. The modern best estimate of ECS is ~3℃ per doubling of CO_2[15], which would produce ~0.41-0.48 ℃ warming from the marine N_2O forcing during the PETM (Extended Data Fig. S6). Previous studies have argued that ECS during the PETM might be higher than modern estimation [51-53], although these estimates did not account for the warming contribution from N_2O. Using a broad ECS range of 2.5-9 ℃, our calculations show that the marine N_2O forcing produces ~0.3-1.4 ℃ of additional warming, with only a modest dependence on the assumed PETM background CO_2 and CH_4 levels (Extended Data Fig. S6).

N_2O-induced warming was calculated as follows:

For a steady-state atmosphere, the perturbation in N_2O concentration (ΔC, ppb) due to enhanced marine nitrification was estimated from the emission change (ΔE, Tg N yr^{-1}) as:

$$\Delta C = \frac{\Delta E \times \tau}{2.14}$$

where $\tau = 116\ yr$ is the atmospheric lifetime of N_2O and 2.14 Tg N ppb^{-1} is the mass-to-mixing ratio conversion factor.

The stratospheric-temperature-adjusted radiative forcing (SARF) of N_2O was calculated following the IPCC AR6 parameterization[75]:

$$SARF_{N_2O} = (a_2\sqrt{C} + b_2\sqrt{N} + c_2\sqrt{M} + d_2)(\sqrt{N} - \sqrt{N_0})$$

where C, M, N are the concentrations of CO_2 (ppm), CH_4 (ppb), and N_2O (ppb), and $N_0 = 273.87\ ppb$. The coefficients are $a_2 = -3.4197 \times 10^{-4}$, $b_2 = 2.5455 \times 10^{-4}$, $c_2 = -2.4357 \times 10^{-4}$, and $d_2 = 0.12173$

The effective radiative forcing (ERF) was obtained through tropospheric adjustment for SARF as:

$$ERF_{N_2O} = 1.07 \times SARF_{N_2O}$$

following the AR6 convention.

The marginal forcing was then calculated as

$$\Delta F_{N_2O} = ERF\big(C, M, N_{bg} + \Delta C\big) - ERF(C, M, N_{bg})$$

where $N_{bg}$is the Eocene background N_2O level. Because the Eocene background N_2O is underconstrained, we tested a range between 270-600ppb.

Finally, the global mean temperature response was estimated assuming

$$\Delta T = \frac{ECS}{3.7} \times \Delta F_{N_2O}$$

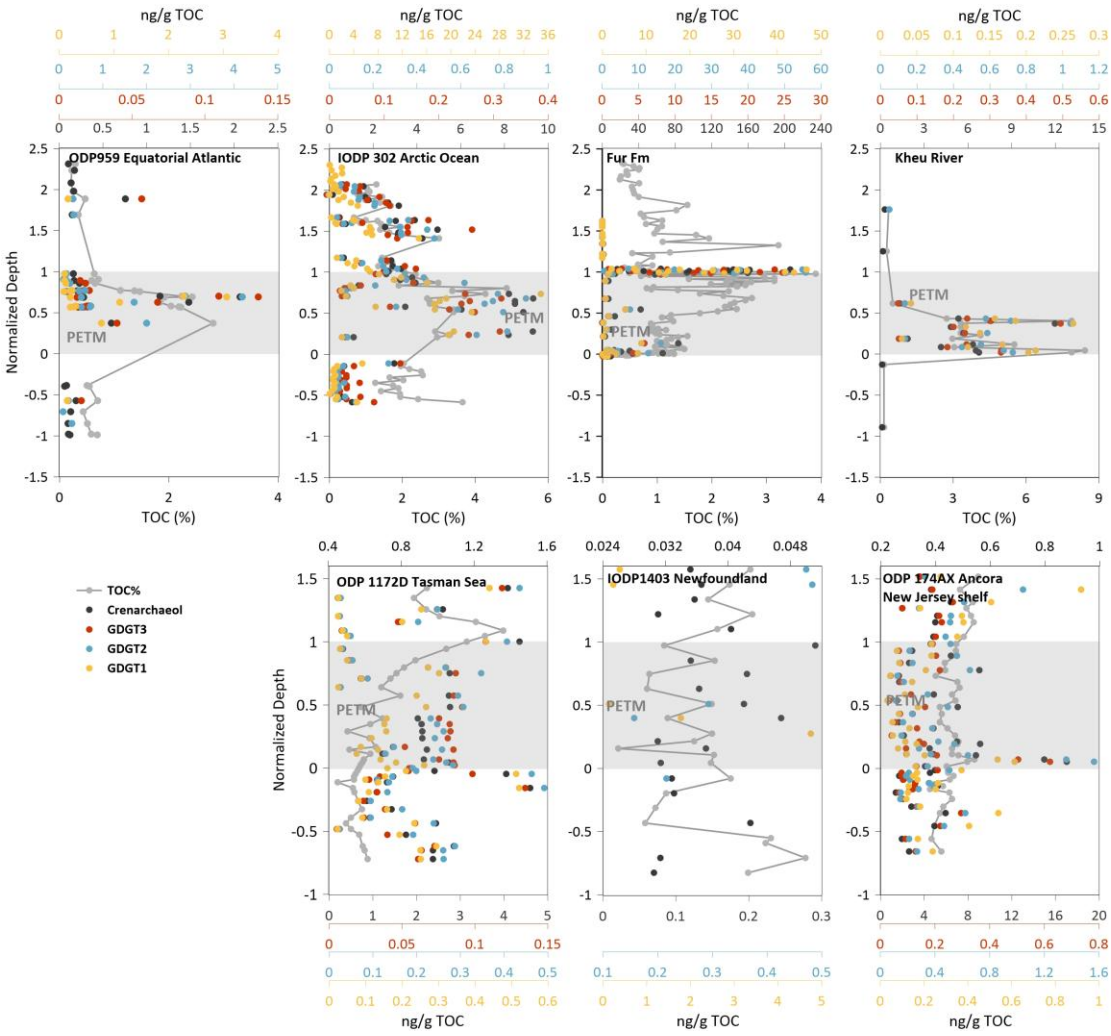

Extended Data Fig. S1 Changes in total organic carbon (TOC) and archaeal membrane lipids (normalized to TOC) across the PETM. The grey lines trace TOC (%). Colored dots are individual samples of crenarchaeol and GDGT1–3 (ng/g TOC). The y-axis is normalized depth, assuming constant sedimentation rate, 0 marks the PETM onset and the grey shading denotes the PETM interval. Please note the different scaling of the x-axes.

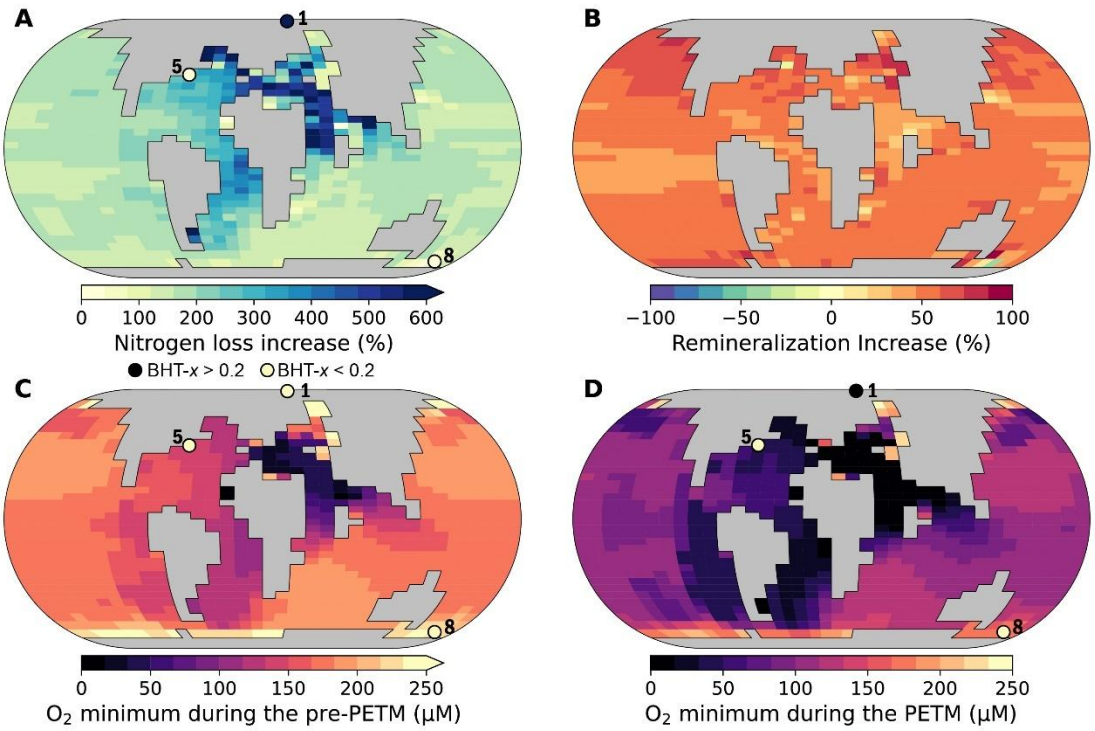

Extended Data Fig. S2 Proxy- and cGENIE model-based reconstructions of changes in marine oxygen and nitrogen cycling during the PETM relative to pre-PETM conditions. A, Proxy- and model-based percent increase of water-column integrated nitrogen loss; **B**, Modelled percent increase of water-column integrated organic matter remineralization; **C**, Proxy- and model-based minimum oxygen concentrations before the PETM and **D**, during the body PETM. Minimum oxygen concentrations are shown as the lowest water-column values at each grid cell. Grey shading indicates land areas. Black and yellow circles mark core sites discussed in the text, where black circles indicate BHT-x > 0.2 and yellow circles indicate BHT-x < 0.2. Numbers refer to sampling sites: 1. Arctic Ocean (IODP 302); 5. New Jersey Shelf (ODP 174AX Ancora); 8. Tasman Sea (ODP 1172). The Arctic Ocean is masked, as the model configuration does not resolve physical circulation appropriately in this region.

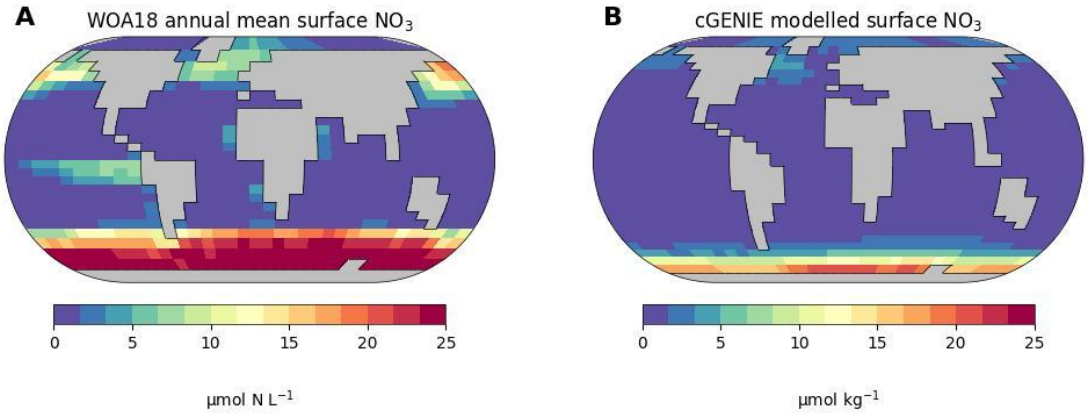

Extended Data Fig. S3 Comparison of modern surface nitrate concentration between A, observation from World Ocean Atlas 2018, and B, cGENIE modelled pre-industrial results with modern geography (1× CO2, 1× PO43-). The global, volume-weighted comparison of simulated and observed nitrate yields an M-score of 0.74.

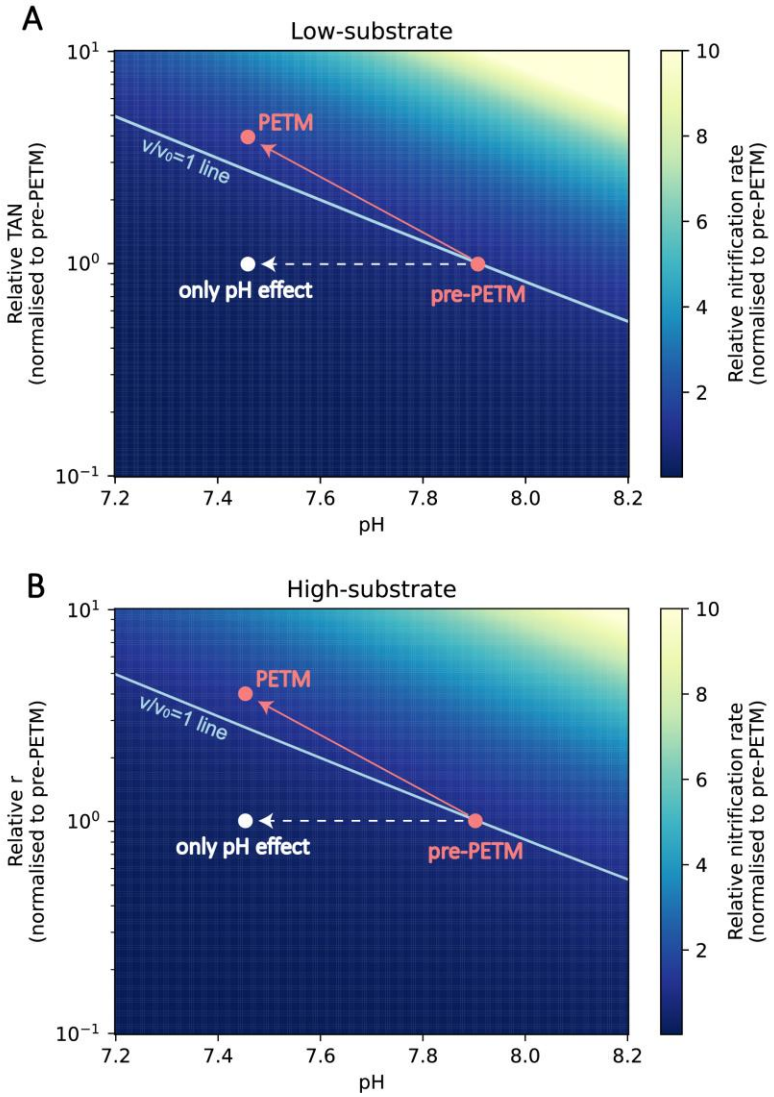

Extended Data Fig. S4 Rate response of marine ammonia oxidation to pH and substrate supply. A, Low-substrate scenario ($[NH_3] << K_m$), where v/v_0 is proportional to TAN/TAN_0. Heat map shows the relative nitrification rate (in color scale, normalized to pre-PETM) as a function of pH (x-axis) and relative total ammonia nitrogen (TAN, y-axis, log scale) under the low-substrate. The cyan line marks the relative nitrification rate equals to 1 isoline. Red markers denote the pre-PETM and PETM states. The white dashed arrow indicates the change expected from only pH decrease alone at constant TAN. The red arrow illustrates the combined trajectory of acidification and TAN increase from the pre-PETM reference (right) to the inferred PETM state (left). **B**, Full Michaelis–Menten formulation with NH_3 as the substrate. The surface shows the ammonia oxidation rate (equal to nitrification rate due to rate-limitation of nitrification by ammonia oxidation) relative to the pre-PETM (v/v_0) as function of pH and $\log_{10}(r/r_0)$, where $r=TAN/K_m$. Color bar indicates v/v_0. y-axes are plotted on a $\log_{10}$ scale.

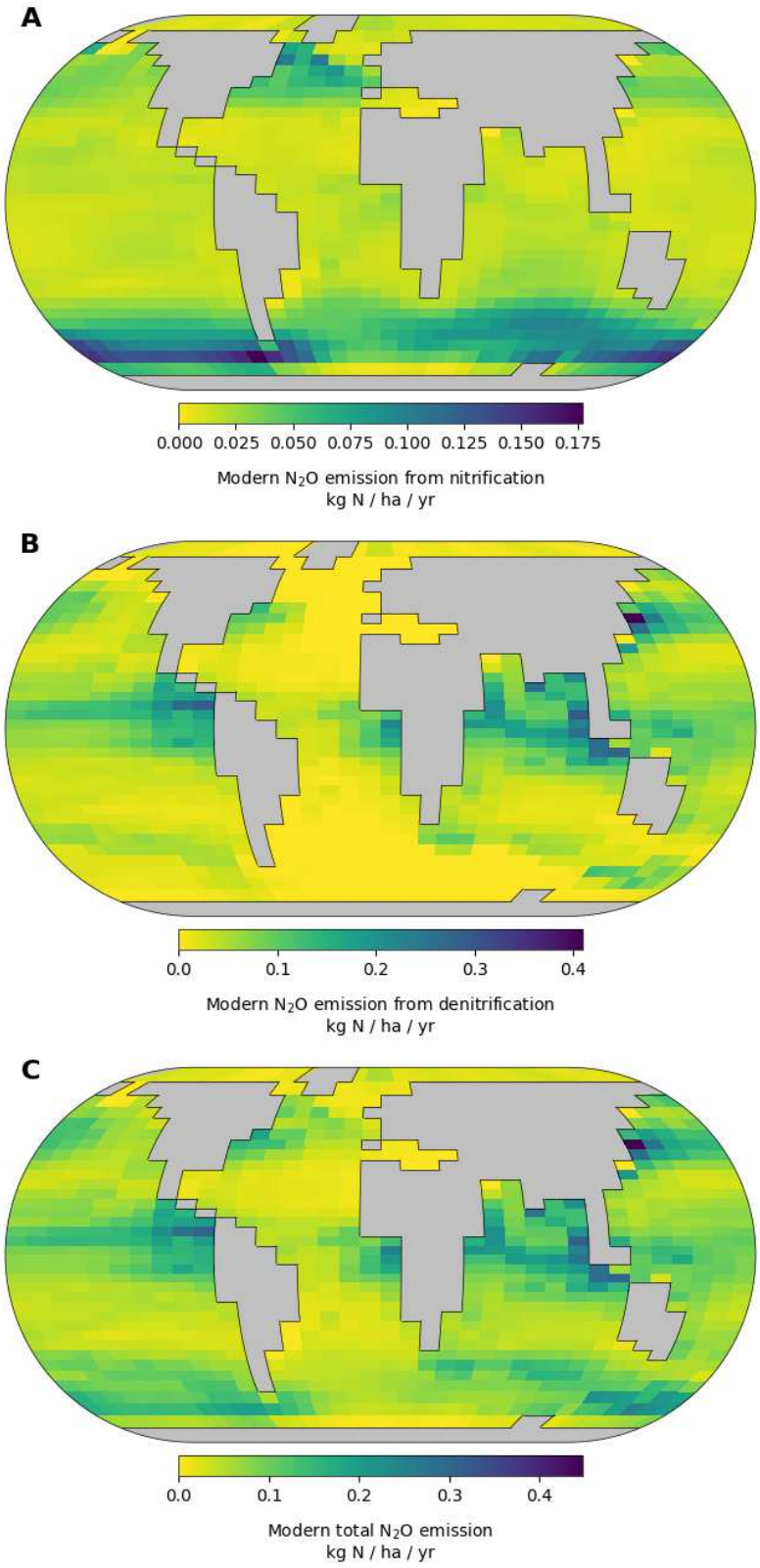

Extended Data Fig. S5 cGENIE model estimation of modern marine N_2O emission (kg N ha^{-1} yr^{-1}; ha: hectare). A, Modelled pre-industrial N_2O flux from nitrification under modern geography and baseline boundary conditions (1× CO_2, 1× PO_4^{3-}). This result is consistent with observational estimates by ref. [50]; **B**, Modelled

pre-industrial N_2O flux from denitrification under modern geography and baseline boundary conditions. **C**, Modelled pre-industrial N_2O flux combining nitrification and denitrification under modern geography and baseline boundary conditions.

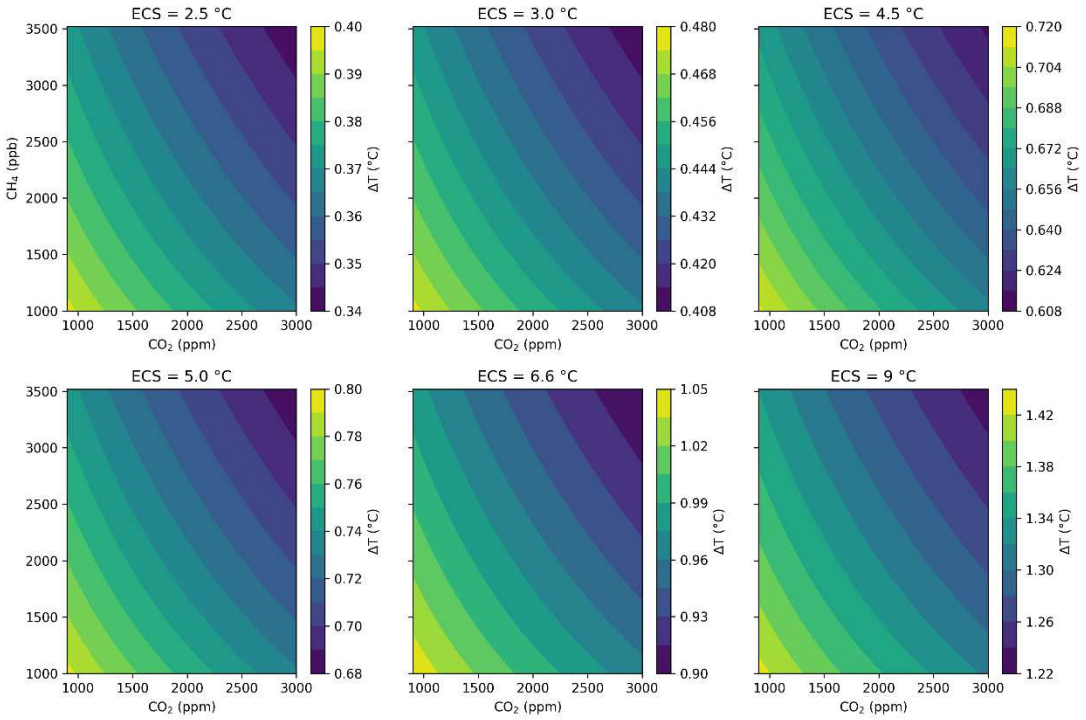

Extended Data Fig. S6 Sensitivity test of global temperature change (ΔT) resulting from a 3.6 Tg N yr^{-1} increase in marine-derived N_2O emissions, evaluated across background CO_2 (900–3000 ppm), CH_4 (1000–3500 ppb), and a range of equilibrium climate sensitivities (ECS)[53] under 2.5°C, 3°C, 4.5°C, 5°C, 6.6°C, 9°C. Radiative forcing follows the IPCC AR6 N_2O formulation[75] with an atmospheric lifetime of 116 yr and background N_2O = 288 ppb. Higher ECS increases ΔT proportionally, while higher CO_2 and CH_4 slightly weaken the marginal N_2O forcing due to spectral overlap, yielding ΔT values of ~0.3–1.4 °C across the tested parameter space.

Extended Data Table 1. Additional information on study sites. Paleolocations are based on DeepMIP-Eocene geography [76]

Site	Present-day location	Latitude and longitude	Paleolatitude and paleolongitude	Paleodepth	Dry bulk density
IODP 302-M0004	Lomonosov Ridge, Central Arctic Ocean	~87.87°N, 136.18°E	82.9°N, 29.5°E	200 m[77]	1.38
ODP Site 1172	East Tasman Plateau, Southwest Pacific Ocean	44.95°S, 150.92°E	65.1°S, 161.4°E	300 m[78]	1.2
Kheu River	Central Northern Caucasus	43.7°N, 43.38°E	42.0°N, 38.5°E	100–200 m[79]	2.4 for shale[61]
ODP 174AX Ancora	New Jersey Shelf, Atlantic Coastal Plain	39.69°N, 74.85°W	38.2°N, 56°W	< 110 m[80]	1.8
ODP 959	Côte d'Ivoire–Ghana Transform Margin, equatorial Atlantic	3.63° N, 2.74° W	3.1°S, 8.2°W	~1000 m[81]	1.55
IODP 1403	Southeast Newfoundland Ridge, central North Atlantic	39.94°N, 51.80°W	35.4°N, 34.5°W	~4374 m[82]	1.63
Fur Fm	Fur island, Denmark	56.84° N, 8.10° E	52.5°N,4.1°E	100-200 m[83]	1.4 and 0.8[84]
Qimugen Fm	Tarim Basin, West China	39.85°N, 74.50°E	40.9°N, 70.8°E	< 100 m[85]	-

Extended Data Table 2 Detection of BHT-x at studied sites during the PETM.

Summary of BHT-*x* detection across all investigated sites. “Detected” indicates measurable BHT-*x* presence; “N.D.” = not detected; “Not measured” = sample not analyzed due to insufficient material.

Site	BHT-*x* detection
IODP 302-M0004	Detected
ODP Site 1172	Detected
Kheu River	N.D
ODP 174AX Ancora	Detected
ODP 959	N.D
IODP 1403	N.D
Fur Fm	N.D
Qimugen Fm	Not measured

References

1 McInerney, F. A. & Wing, S. L. The Paleocene-Eocene Thermal Maximum: A Perturbation of Carbon Cycle, Climate, and Biosphere with Implications for the Future. *Annual Review of Earth and Planetary Sciences* **39**, 489–516, doi:10.1146/annurev-earth-040610-133431 (2011).

2 Westerhold, T. *et al.* An astronomically dated record of Earth's climate and its predictability over the last 66 million years. *Science* **369**, 1383–1387 (2020).

3 Babila, T. L. *et al.* Capturing the global signature of surface ocean acidification during the Palaeocene–Eocene Thermal Maximum. *Philosophical Transactions of the Royal Society A: Mathematical, Physical and Engineering Sciences* **376**, 20170072 (2018).

4 Gutjahr, M. *et al.* Very large release of mostly volcanic carbon during the Palaeocene-Eocene Thermal Maximum. *Nature* **548**, 573–577, doi:10.1038/nature23646 (2017).

5 Penman, D. E., Hönisch, B., Zeebe, R. E., Thomas, E. & Zachos, J. C. Rapid and sustained surface ocean acidification during the Paleocene - Eocene Thermal Maximum. *Paleoceanography* **29**, 357–369 (2014).

6 Behrooz, L. *et al.* North-East Peri-Tethyan Water Column Deoxygenation and Euxinia at the Paleocene Eocene Thermal Maximum. *Paleoceanography and Paleoclimatology* **39**, 1–20, doi:10.1029/2023pa004828 (2024).

7 Yao, W., Paytan, A. & G. Wortmann, U. Large-scale ocean deoxygenation during the Paleocene-Eocene Thermal Maximum. *Science* **361**, 804–806 (2018).

8 Dickson, A. J., Cohen, A. S. & Coe, A. L. Seawater oxygenation during the Paleocene-Eocene thermal maximum. *Geology* **40**, 639–642 (2012).

9 Santoro, A. E., Buchwald, C., McIlvin, M. R. & Casciotti, K. L. Isotopic signature of N_2O produced by marine ammonia-oxidizing archaea. *Science* **333**, 1282–1285, doi:10.1126/science.1208239 (2011).

10 Martens-Habbena, W., Berube, P. M., Urakawa, H., R. de la Torre, J. & A. Stahl, D. Ammonia oxidation kinetics determine niche separation of nitrifying Archaea and Bacteria. *Nature* **461**, 976–979, doi:10.1038/nature08465 (2009).

11 Beman, J. M. *et al.* Global declines in oceanic nitrification rates as a consequence of ocean acidification. *Proceedings of the National Academy of Sciences* **108**, 208–213, doi:10.1073/pnas.1011053108 (2011).

12 Gruber, N. The marine nitrogen cycle: overview and challenges. in *Nitrogen in the Marine Environment* Vol. 2 1–50 (2008).

13 Gruber, N. & Galloway, J. N. An Earth-system perspective of the global nitrogen cycle. *Nature* **451**, 293–296, doi:10.1038/nature06592 (2008).

14 Yung, Y., Wang, W. & Lacis, A. Greenhouse effect due to atmospheric nitrous oxide. *Geophysical research letters* **3**, 619–621 (1976).

15 Forster, P. *et al.* Chapter 7: The Earth's Energy Budget, Climate Feedbacks, and Climate Sensitivity. in *Climate Change 2021: The Physical Science Basis* (eds V. Masson-Delmotte *et al.*) 923–1054 (Cambridge University Press, 2021).

16 Ward, B. B. Nitrification in Marine Systems. in *Nitrogen in the Marine Environment* 199–261 (2008).

17 Junium, C. K., Dickson, A. J. & Uveges, B. T. Perturbation to the nitrogen cycle during rapid

Early Eocene global warming. *Nat Commun* **9**, 3186, doi:10.1038/s41467-018-05486-w (2018).

18 Moretti, S. *et al.* Oxygen rise in the tropical upper ocean during the Paleocene-Eocene Thermal Maximum. *Science* **383**, 727–731 (2024).

19 Yao, W. *et al.* Expanded subsurface ocean anoxia in the Atlantic during the Paleocene-Eocene Thermal Maximum. *Nat Commun* **15**, 9053, doi:10.1038/s41467-024-53423-x (2024).

20 Knies. Surface water productivity and paleoceanographic implications in the Cenozoic Arctic. *Paleoceanography*, doi:10.1029/2007PA001455 (2008).

21 Sigman, D. M. & Fripiat, F. Nitrogen Isotopes in the Ocean. in *Encyclopedia of Ocean Sciences* 263–278 (2019).

22 Elling, F. J. *et al.* Chemotaxonomic characterisation of the thaumarchaeal lipidome. *Environ Microbiol* **19**, 2681–2700, doi:10.1111/1462-2920.13759 (2017).

23 Wuchter, C. *et al.* Archaeal nitrification in the ocean. *Proceedings of the National Academy of Sciences* **103**, 12317–12322 (2006).

24 Kim, J.-G. *et al.* Hydrogen peroxide detoxification is a key mechanism for growth of ammonia-oxidizing archaea. *Proceedings of the National Academy of Sciences* **113**, 7888–7893 (2016).

25 Könneke, M. *et al.* Ammonia-oxidizing archaea use the most energy-efficient aerobic pathway for CO_2 fixation. *Proceedings of the National Academy of Sciences* **111**, 8239–8244, doi:10.1073/pnas.1402028111 (2014).

26 Monteiro, F. M., Pancost, R. D., Ridgwell, A. & Donnadieu, Y. Nutrients as the dominant control on the spread of anoxia and euxinia across the Cenomanian-Turonian oceanic anoxic event (OAE2): Model-data comparison. *Paleoceanography* **27**, doi:10.1029/2012pa002351 (2012).

27 Rush, D. *et al.* Anaerobic ammonium-oxidising bacteria: A biological source of the bacteriohopanetetrol stereoisomer in marine sediments. *Geochimica et Cosmochimica Acta* **140**, 50–64, doi:10.1016/j.gca.2014.05.014 (2014).

28 Sáenz, J. P., Wakeham, S. G., Eglinton, T. I. & Summons, R. E. New constraints on the provenance of hopanoids in the marine geologic record: Bacteriohopanepolyols in marine suboxic and anoxic environments. *Organic Geochemistry* **42**, 1351–1362, doi:10.1016/j.orggeochem.2011.08.016 (2011).

29 Schwartz-Narbonne, R. *et al.* A unique bacteriohopanetetrol stereoisomer of marine anammox. *Organic Geochemistry* **143**, doi:10.1016/j.orggeochem.2020.103994 (2020).

30 van Kemenade , Z. R. *et al.* Bacteriohopanetetrol-*x*: constraining its application as a lipid biomarker for marine anammox using the water column oxygen gradient of the Benguela upwelling system. *Biogeosciences* **19**, 201–221, doi:10.5194/bg-19-201-2022 (2022).

31 R. C. Remmelzwaal, S. *et al.* Investigating Ocean Deoxygenation During the PETM Through the Cr. *Paleoceanography and Paleoclimatology* **34**, 917–929, doi:10.1029/2018PA003372 (2019).

32 Fuchsman, C. A., Murray, J. W. & Konovalov, S. K. Concentration and natural stable isotope profiles of nitrogen species in theBlack Sea. *Marine Chemistry* **111**, 90–105 (2008).

33 Löscher, C. R. *et al.* Water column biogeochemistry of oxygen minimum zones in the

eastern tropical North Atlantic and eastern tropical South Pacific oceans. *Biogeosciences* **13**, 3585–3606 (2016).

34 Bristow, L. A. *et al.* Ammonium and nitrite oxidation at nanomolar oxygen concentrations in oxygen minimum zone waters. *Proceedings of the National Academy of Sciences* **113**, 10601–10606 (2016).

35 Sun, X., Ji, Q., Jayakumar, A. & Ward, B. B. Dependence of nitrite oxidation on nitrite and oxygen in low-oxygen seawater. *Geophysical Research Letters* **44**, 7883–7891 (2017).

36 Lam, P. *et al.* Linking crenarchaeal and bacterial nitrification to anammox in the Black Sea. *Proceedings of the National Academy of Sciences* **104**, 7104–7109 (2007).

37 Löscher, C. R. *et al.* Production of oceanic nitrous oxide by ammonia-oxidizing archaea. *Biogeosciences* **9**, 2419–2429 (2012).

38 Lam, P. & Kuypers, M. M. Microbial nitrogen cycling processes in oxygen minimum zones. *Annual review of marine science* **3**, 317–345 (2011).

39 Lipschultz, F. *et al.* Bacterial transformations of inorganic nitrogen in the oxygen-deficient waters of the Eastern Tropical South Pacific Ocean. *Deep Sea Research Part A. Oceanographic Research Papers* **37**, 1513–1541 (1990).

40 Carmichael, M. J. *et al.* Hydrological and associated biogeochemical consequences of rapid global warming during the Paleocene-Eocene Thermal Maximum. *Global and Planetary Change* **157**, 114–138, doi:10.1016/j.gloplacha.2017.07.014 (2017).

41 Papadomanolaki, N. M. Eutrophication and Deoxygenation Forcing of Marginal Marine Organic. *Paleoceanog and Paleoclimatology* doi:10.1029/2021PA004232 (2022).

42 Naafs, B. D. A. *et al.* Fundamentally different global marine nitrogen cycling in response to severe ocean deoxygenation. *Proceedings of the National Academy of Sciences* **116**, 24979–24984, doi:10.1073/pnas.1905553116 (2019).

43 Suzuki, I., Dular, U. & Kwok, S. Ammonia or ammonium ion as substrate for oxidation by Nitrosomonas europaea cells and extracts. *Journal of Bacteriology* **120**, 556–558 (1974).

44 Wannicke, N., Frey, C., Law, C. S. & Voss, M. The response of the marine nitrogen cycle to ocean acidification. *Glob Chang Biol* **24**, 5031–5043, doi:10.1111/gcb.14424 (2018).

45 Li, M. *et al.* Coupled decline in ocean pH and carbonate saturation during the Palaeocene–Eocene Thermal Maximum. *Nature Geoscience* **17**, 1299–1305, doi:10.1038/s41561-024-01579-y (2024).

46 Schilt, A. *et al.* Glacial–interglacial and millennial-scale variations in the atmospheric nitrous oxide concentration during the last 800,000 years. *Quaternary Science Reviews* **29**, 182–192 (2010).

47 Frame, C. H., Lau, E., Nolan IV, E. J., Goepfert, T. J. & Lehmann, M. F. Acidification enhances hybrid N_2O production associated with aquatic ammonia-oxidizing microorganisms. *Frontiers in microbiology* **7**, 2104 (2017).

48 Goreau, T. J. *et al.* Production of NO_2^- and N_2O by nitrifying bacteria at reduced concentrations of oxygen. *Applied and environmental microbiology* **40**, 526–532 (1980).

49 Ulloa, O., Canfield, D. E., DeLong, E. F., Letelier, R. M. & Stewart, F. J. Microbial oceanography of anoxic oxygen minimum zones. *Proceedings of the National Academy of Sciences* **109**, 15996–16003 (2012).

50 Wang, S. *et al.* Global mapping of flux and microbial sources for oceanic N_2O. *Nat*

Commun **16**, 3341, doi:10.1038/s41467-025-58715-4 (2025).

51 Anagnostou, E. *et al.* Proxy evidence for state-dependence of climate sensitivity in the Eocene greenhouse. *Nature communications* **11**, 4436 (2020).

52 Tierney, J. E. *et al.* Spatial patterns of climate change across the Paleocene–Eocene Thermal Maximum. *Proceedings of the national academy of sciences* **119**, e2205326119 (2022).

53 Zhu, J., Poulsen, C. J. & Tierney, J. E. Simulation of Eocene extreme warmth and high climate sensitivity through cloud feedbacks. *Science advances* **5**, eaax1874 (2019).

54 Ji, Q., Buitenhuis, E., Suntharalingam, P., Sarmiento, J. L. & Ward, B. B. Global nitrous oxide production determined by oxygen sensitivity of nitrification and denitrification. *Global Biogeochemical Cycles* **32**, 1790–1802 (2018).

55 Harris, E. *et al.* Denitrifying pathways dominate nitrous oxide emissions from managed grassland during drought and rewetting. *Science advances* **7**, eabb7118 (2021).

56 Zeebe, R. E., Zachos, J. C. & Dickens, G. R. Carbon dioxide forcing alone insufficient to explain Palaeocene–Eocene Thermal Maximum warming. *Nature Geoscience* **2**, 576–580, doi:10.1038/ngeo578 (2009).

57 Inglis, G. N. *et al.* Global mean surface temperature and climate sensitivity of the EECO, PETM and latest Paleocene. *Climate of the past Discussions* **2020**, 1–43 (2020).

58 Steinig, S. *et al.* DeepMIP-Eocene-p1: multi-model dataset and interactive web application for Eocene climate research. *Scientific Data* **11**, 970 (2024).

59 Yool, A., Martin, A. P., Fernández, C. & Clark, D. R. The significance of nitrification for oceanic new production. *Nature* **447**, 999–1002 (2007).

60 Hollingsworth, E. H. *et al.* Spatial and Temporal Patterns in Petrogenic Organic Carbon Mobilization During the Paleocene-Eocene Thermal Maximum. *Paleoceanography and Paleoclimatology* **39**, doi:10.1029/2023pa004773 (2024).

61 Kaya, M. Y. *et al.* The Eurasian epicontinental sea was an important carbon sink during the Palaeocene-Eocene thermal maximum. *Communications Earth & Environment* **3**, 124, doi:10.1038/s43247-022-00451-4 (2022).

62 Stokke, E. W., Jones, M. T., Tierney, J. E., Svensen, H. H. & Whiteside, J. H. Temperature changes across the Paleocene-Eocene Thermal Maximum–a new high-resolution TEX_{86} temperature record from the Eastern North Sea Basin. *Earth and Planetary Science Letters* **544**, 116388 (2020).

63 Elling, F. J. *et al.* Linking diatom-diazotroph symbioses to nitrogen cycle perturbations and deep-water anoxia: Insights from Mediterranean sapropel events. *Earth and Planetary Science Letters* **571**, 117110, doi:10.1016/j.epsl.2021.117110 (2021).

64 Becker, K. W., Lipp, J. S., Zhu, C., Liu, X.-L. & Hinrichs, K.-U. An improved method for the analysis of archaeal and bacterial ether core lipids. *Organic Geochemistry* **61**, 34–44, doi:10.1016/j.orggeochem.2013.05.007 (2013).

65 Hopmans, E. C., Schouten, S. & Sinninghe Damsté, J. S. The effect of improved chromatography on GDGT-based palaeoproxies. *Organic Geochemistry* **93**, 1–6, doi:10.1016/j.orggeochem.2015.12.006 (2016).

66 Beman, J. M., Popp, B. N. & Francis, C. A. Molecular and biogeochemical evidence for ammonia oxidation by marine Crenarchaeota in the Gulf of California. *The ISME Journal*

2, 429–441 (2008).

67 Tang, W. *et al.* Database of nitrification and nitrifiers in the global ocean. *Earth System Science Data* **15**, 5039–5077, doi:10.5194/essd-15-5039-2023 (2023).

68 Meyer, V. D. *et al.* Dominant control of temperature on (sub-) tropical soil carbon turnover. *Nature Communications* **16**, 4530 (2025).

69 Hopmans, E. C., Smit, N. T., Schwartz-Narbonne, R., Sinninghe Damsté, J. S. & Rush, D. Analysis of non-derivatized bacteriohopanepolyols using UHPLC-HRMS reveals great structural diversity in environmental lipid assemblages. *Organic Geochemistry* **160**, doi:10.1016/j.orggeochem.2021.104285 (2021).

70 Elling, F. J. *et al.* Archaeal lipid biomarker constraints on the Paleocene-Eocene carbon isotope excursion. *Nat Commun* **10**, 4519–4529, doi:10.1038/s41467-019-12553-3 (2019).

71 Polik, C. A., Elling, F. J. & Pearson, A. Impacts of Paleoecology on the TEX_{86} Sea Surface Temperature Proxy in the Pliocene-Pleistocene Mediterranean Sea. *Paleoceanography and Paleoclimatology* **33**, 1472–1489, doi:10.1029/2018pa003494 (2018).

72 Ridgwell, A. *et al.* Marine geochemical data assimilation in an efficient Earth System Model of global biogeochemical cycling. *Biogeosciences* **4**, 87–104 (2007).

73 Reinhard, C. T. *et al.* Oceanic and atmospheric methane cycling in the cGENIE Earth system model–release v0. 9.14. *Geoscientific Model Development* **13**, 5687–5706 (2020).

74 Canadell, J. G. *et al.* Global Carbon and other Biogeochemical Cycles and Feedbacks. in *Climate Change 2021: The Physical Science Basis. Contribution of Working Group I to the Sixth Assessment Report of the Intergovernmental Panel on Climate Change* (eds V. Masson-Delmotte *et al.*) 673–816 (Cambridge University Press, 2021).

75 Change, I. P. o. C. Supplementary Material for Chapter 7: The Earth's Energy Budget, Climate Feedbacks, and Climate Sensitivity. (Cambridge University Press, Cambridge, United Kingdom and New York, NY, USA, 2021).

76 Herold, N. *et al.* A suite of early Eocene (~ 55 Ma) climate model boundary conditions. *Geoscientific Model Development* **7**, 2077–2090 (2014).

77 Sluijs, A. *et al.* Arctic late Paleocene–early Eocene paleoenvironments with special emphasis on the Paleocene-Eocene thermal maximum (Lomonosov Ridge, Integrated Ocean Drilling Program Expedition 302). *Paleoceanography* **23** (2008).

78 Hollis, C. J. *et al.* The DeepMIP contribution to PMIP4: Methodologies for selection, compilation and analysis of latest Paleocene and early Eocene climate proxy data, incorporating version 0.1 of the DeepMIP database. *Geoscientific Model Development* **12**, 3149–3206 (2019).

79 Gavrilo, Y. O., Shcherbinina, E. A. & Oberhänsli, H. Paleocene-Eocene boundary events in the northeastern Peri-Tethys. in *Causes and consequences of globally warm climates in the early Paleogene* (eds Scott L. Wing, Philip D. Gingerich, Birger Schmitz, & Ellen Thomas) (2003).

80 Harris, A. D. *et al.* Integrated stratigraphic studies of Paleocene–lowermost Eocene sequences, New Jersey Coastal Plain: Evidence for glacioeustatic control. *Paleoceanography* **25** (2010).

81 Frieling, J. *et al.* Tropical Atlantic climate and ecosystem regime shifts during the

Paleocene–Eocene Thermal Maximum. *Climate of the Past* **14**, 39–55 (2018).

82 Penman, D. E. *et al.* An abyssal carbonate compensation depth overshoot in the aftermath of the Palaeocene–Eocene Thermal Maximum. *Nature Geoscience* **9**, 575–580 (2016).

83 Schoon, P. L., Heilmann-Clausen, C., Schultz, B. P., Sinninghe Damsté, J. S. & Schouten, S. Warming and environmental changes in the eastern North Sea Basin during the Palaeocene–Eocene Thermal Maximum as revealed by biomarker lipids. *Organic Geochemistry* **78**, 79–88, doi:10.1016/j.orggeochem.2014.11.003 (2015).

84 Jones, M. T. *et al.* Tracing North Atlantic volcanism and seaway connectivity across the paleocene–eocene thermal maximum (PETM). *Climate of the Past* **19**, 1623–1652 (2023).

85 Kaya, M. Y. *et al.* Paleogene evolution and demise of the proto-Paratethys Sea in Central Asia (Tarim and Tajik basins): Role of intensified tectonic activity at ca. 41 Ma. *Basin Research* **31**, 461–486, doi:10.1111/bre.12330 (2019).

Supplementary Files

This is a list of supplementary files associated with this preprint. Click to download.

- SupplementaryMaterialsfor.docx